

Submitted to *The Astrophysical Journal*

## Monte Carlo Simulations of Thermal-Nonthermal Radiation from a Neutron Star Magnetospheric Accretion Shell

Markus Böttcher<sup>1,2</sup> and Edison P. Liang<sup>2</sup>

### ABSTRACT

We discuss the space-and-time-dependent Monte Carlo code we have developed to simulate the relativistic radiation output from compact astrophysical objects, coupled to a Fokker-Planck code to determine the self-consistent lepton populations. We highlight some major recent results obtained with this code,. They are relevant to the emission from a magnetized neutron star accretion shell near the Alfvén radius, reprocessing the radiation from the neutron star surface. We explore the parameter space defined by the accretion rate, stellar surface field and the level of wave turbulence in the shell.

### 1. Introduction

The high energy radiation from compact astrophysical objects is emitted by relativistic or semi-relativistic thermal and nonthermal leptons (electrons and pairs) via synchrotron, bremsstrahlung, and Compton processes, plus bound-bound and bound-free transitions of high-Z elements. Since Compton scattering is a dominant radiation mechanism in this regime, the most efficient and accurate method to model the transport of high energy radiation is the Monte Carlo (MC) technique. During the past decade we have developed a versatile state-of-the-art space-and-time-dependent MC code to model the radiative output of compact objects (see e.g. Liang et al 2000). Recently we have added the self-consistent evolution of the leptons using a Fokker-Planck scheme. The lepton evolution is then coupled to the photon transport. Here we apply this coupled MC-FP code to the study of the reprocessing of blackbody radiation from a weakly magnetized neutron star surface by a magnetized spherical shell at the Alfvén radius.

Because of the 1-D nature of our code at this stage, the neutron star is assumed to emit isotropic blackbody radiation, the reprocessing magnetospheric plasma is idealized as part of a spherical shell at the Alfvén radius, and the magnetic field is taken to be nondirectional, so

---

<sup>1</sup>Chandra Fellow

<sup>2</sup>Physics and Astronomy Department, Rice University, MS 108, 6100 S. Main Street, Houston, TX 77005-1892, USA

that the radiation output is isotropic. Even though this is not a perfect representation of a quasi-dipolar magnetosphere and accretion flow, we believe that, except for very special viewing angles, our output spectra should be a reasonable approximation to the angle-averaged output of the reprocessing by a hybrid thermal/nonthermal magnetosphere.

To highlight the capability of our code, we assume that the leptons are energized by Coulomb collisions with virial ions and accelerated nonthermally by Alfvén and whistler wave turbulence, and cooled by cyclotron/synchrotron, bremsstrahlung, and inverse Comptonization of both internal soft photons and blackbody photons from the stellar surface. The lepton and photon distributions are evolved together self-consistently until they reach steady-state.

Recent observations of weak-field neutron star binaries (e.g., Tavani et al. 1996) indicate that many exhibit soft (photon index  $> 2.2$ ) power law tails extending beyond 100 keV, at least episodically, in addition to the keV thermal component which presumably originates from the stellar surface. The origin of this high energy tail is unexplained at present. It could be due to thermal Comptonization by a hot coronal plasma, or it could be due to nonthermal emission. Tavani and Liang (1996) examined systematically the possible sites of nonthermal emissions and concluded that the Alfvén surface is the most likely candidate since the dissipation of the rotation energy of the disk is strongest there, due to magnetic reconnection and wave turbulence generation. Here we first focus on particle acceleration by wave turbulence.

## 2. Physics of photon and lepton evolution

We use the Monte Carlo (MC) technique (Podznyakov et al 1984, Canfield et al 1987, Liang 1993, Hua et al 1997) to simulate relativistic photon transport. We include the full (energy-and-angle-dependent) Klein-Nishina cross section for Comptonization, relativistic bremsstrahlung from lepton-ion and lepton-lepton scattering (Dermer 1984), and cyclo-synchrotron processes (Brainerd 1984) in magnetic fields. The MC photon transport is fully space-and-time-dependent. Photons are born with a certain "weight" which is diminished by absorption and escape, until the weight drops below a user-specified limit, at which point the photon is "killed". Surviving photons are sampled at boundaries to provide time-and-frequency-dependent spectral output. In addition to self-emitted photons from the plasma, soft photons can be injected at zone boundaries and inside volume elements. Currently the code can handle 1-D spherical, cylindrical or slab geometries with an arbitrary number of spatial zones. However since the photon ray tracing is done with full angle informations, the generalization to 2-and-3-D transport is straight forward. The maximum number of photon frequency bins is 128. For more details of this code see Canfield et al (1987) and Böttcher & Liang (1998). A typical MC run with a million particles at a Thomson depth of a few takes 10s of minutes on a DEC alpha server. Since the CPU time usage scales as the square of the Thomson depth ( number of scatterings), Thomson thick runs can be quite time consuming. We are currently developing a random walk scheme for Wien photons trapped in Thomson thick zones, which would save large amounts of CPU time without introducing too much error.

The lepton population is computed locally in each spatial zone using the Fokker-Planck approximation (Dermer et al 1996, Li et al 1996), taking into account coulomb and Moller scattering, stochastic acceleration by Alfvén and whistler wave turbulence, and radiative cooling (plus pair processes if necessary). In general the lepton population consists of a low energy thermal population plus a high-energy tail truncated at the highest energies by radiative cooling. The photon and lepton evolutions are coupled to each other via a quasi-implicit time scheme in which we use an average of the photon-electron energy exchange rates between two subsequent time steps to compute the electron cooling rates, in particular due to Compton scattering. The Fokker-Planck equation governing the electron evolution is solved using a fully implicit scheme. In contrast to several other codes currently used in the literature (e.g., Stern et al. 1995; Li, Kusunose & Liang 1996, Malzac & Jourdain 2000), we solve the evolution of the entire electron population with the FP scheme and do not introduce any artificial separation between thermal and non-thermal particles. Since the lepton distribution typically evolves much faster than the photon distribution, each photon cycle contains many lepton cycles. The user, however, can always turn off the nonthermal lepton acceleration and assume a strict thermal population whose temperature can be computed self-consistently from energy balance alone.

In order to calculate the emissivities and opacities for thermal cyclotron, non-thermal synchrotron, and thermal bremsstrahlung emission (and only for this purpose), the electron distribution calculated with our Fokker-Planck scheme is decomposed into a thermal population plus a non-thermal tail. For the thermal bremsstrahlung and non-thermal synchrotron emission and absorption, the standard expressions from Rybicki & Lightman (1979) are used. For the thermal cyclotron emission, we add explicitly over the first 5 harmonics, beyond which we use the asymptotic continuum representation of Mahadevan, Narayan & Yi (1996).

Since in many cases of interest to the current investigation the moderately to strongly magnetized coronal plasma is optically thick at low frequencies,  $h\nu \ll 1$  keV, due to synchrotron-(self-)absorption, we use the following simplification in order to save CPU time: For any given frequency  $h\nu \lesssim 1$  keV, we compare the absorption length  $l_{\text{abs}}^\nu$  to the Compton mean free path,  $l_{\text{Compt}}^\nu$  and the radial extent  $\Delta R$  of the current zone of the Comptonizing region. If

$$l_{\text{abs}}^\nu < 0.1 \min \{ l_{\text{Compt}}^\nu, \Delta R \} \quad (1)$$

any soft photon produced at this frequency has a very small probability of escaping the current zone or being up-scattered (to a frequency at which the absorption length will be different so that the above criterion has to be re-evaluated after the scattering event) before being re-absorbed. Thus, in the frequency ranges where Eq. (1) is fulfilled, the radiation escaping at the boundary of that zone will be approximately given by the respective section of the thermal blackbody spectrum. Accordingly, our code neglects the volume emissivities in those frequency ranges and, instead, produces thermal blackbody photons at the zone boundaries.

During each photon time step, the code keeps track of the energy transferred between photons

and electrons due to Compton scattering and cyclotron/synchrotron and bremsstrahlung emission and absorption. The respective heating and cooling rates are used to scale the energy loss/gain coefficients of electrons at a given energy  $E_e = \gamma m_e c^2$ . For the bremsstrahlung energy loss rate, we use the approximate scaling law  $(d\gamma/dt)_{\text{br}} \propto -\gamma^{1.1}$  (Böttcher, Pohl, & Schlickeiser 1999). Coulomb heating/cooling is included using the energy exchange and dispersion rates given in Dermer & Liang (1989). We assume that the ions have a pre-specified temperature  $kT_p \gtrsim 1$  MeV, which is not significantly affected by any changes of the electron temperature. For the energy exchange due to Møller scattering (elastic electron-electron scattering) we use the electron energy exchange and dispersion coefficients given in Nayakshin & Melia (1998).

In addition to Coulomb interactions and radiative losses, we also account for stochastic (2<sup>nd</sup> order Fermi) acceleration due to Alfvén and Whistler waves. For a given background magnetic field  $B$ , the magnitude and spectrum of hydromagnetic plasma wave turbulences are determined by the parameters  $\delta^2 \equiv (\Delta B/B)^2$ , where  $\Delta B$  is the amplitude of the magnetic-field fluctuations, and  $q$ , the spectral index of the turbulence spectrum. We will generally use  $q = 5/3$ , characteristic of Kolmogorov turbulence. The electron acceleration and energy dispersion rates are calculated using the formalism of Schlickeiser (1989). However, we have to take into account that those plasma waves interacting efficiently with the low-energy, quasi-thermal part of the electron spectrum will be efficiently damped and absorbed by the process of Landau damping (e.g., Schlickeiser, Fichtner & Kneller 1996). This leads to a strong truncation of the Kolmogorov wave spectrum above a critical wave number for which the equivalent absorption depth through the region occupied by the hot plasma exceeds unity. We take the effect of Landau damping into account by introducing an effective absorption depth  $\tau_k$  at wave number  $k$ , and correcting the acceleration rate  $\dot{\gamma}_A^0$  of Schlickeiser (1989) due to the “optically thin” plasma wave spectrum by an absorption term:

$$\dot{\gamma}_A = \dot{\gamma}_A^0 \frac{(1 - e^{-\tau_{k_{\text{res}}}})}{\tau_{k_{\text{res}}}}. \quad (2)$$

Here  $\tau_{k_{\text{res}}} = \Gamma_{k_{\text{res}}} t_A$ , and  $\Gamma_k$  is the Landau damping rate at wave number  $k_{\text{res}}$  at which Alfvén waves are resonating preferentially with electrons of energy  $\gamma$ .  $t_A = \Delta R/v_A$  is the Alfvén crossing time of the zone. This modified acceleration term can be renormalized either to correspond to the pre-specified value of  $\delta^2$  for electrons resonating with waves in the weakly damped part of the Alfvén wave spectrum (i.e. at high electron energies), or by specifying a heat input rate into the electron ensemble due to resonant wave/particle interactions.

As an option, our code can account for pair production and annihilation and the corresponding photon absorption and emission. The pair annihilation rates and annihilation radiation emissivities are taken from Svensson (1982), and the  $\gamma\gamma$  pair production rate of Böttcher & Schlickeiser (1997) is used. In addition, simple Compton reflection schemes, using the Green’s functions for reflection off neutral disk material of White, Lightman & Zdziarski (1988) and Lightman & White (1988), can be used to simulate a Compton reflection component either off the inner boundary (corresponding to a quasi-homogeneous slab geometry) or reflecting part of the radiation escaping

at the outer boundary (e.g., corresponding to a cold outer disk).

Assuming local isotropy of the electron distribution, we solve the one-dimensional Fokker-Planck equation

$$\frac{\partial n_e(\gamma, t)}{\partial t} = -\frac{\partial}{\partial \gamma} \left[ n_e(\gamma, t) \frac{d\gamma}{dt} \right] + \frac{1}{2} \frac{\partial^2}{\partial \gamma^2} [n_e(\gamma, t) D(\gamma, t)], \quad (3)$$

where  $D$  is the energy dispersion coefficient. To solve Eq. 3, we use an implicit version of the discretization scheme proposed by Nayakshin & Melia (1998). We choose a logarithmic spacing in electron kinetic energy,  $x_i \equiv \gamma_i - 1$ . In the following the subscript  $i$  refers to electron energy, while the superscript  $n$  refers to time. We define  $f_i^n \equiv n_e(\gamma_i, t^n)/n_e$ . The discretization is then given by

$$f_i^n = f_i^{n+1} + \Delta t \left( \frac{a_{i+1}^{n+1} f_{i+1}^{n+1} - a_{i-1}^{n+1} f_{i-1}^{n+1}}{\Delta x_i + \Delta x_{i-1}} \right) - \Delta t \left( \frac{\alpha D_{i+1}^{n+1} f_{i+1}^{n+1} - 2D_i^{n+1} f_i^{n+1} + \rho D_{i-1}^{n+1} f_{i-1}^{n+1}}{\alpha \Delta x_i (\Delta x_{i-1} + \Delta x_i)} \right), \quad (4)$$

where  $a_i = (d\gamma/dt)(x_i)$ ,  $D_i = [d(\Delta\gamma)^2/dt](x_i)$ ,  $\alpha = 2/(1+q)$ ,  $\rho = 2q/(1+q)$ , with  $q = x_{i+1}/x_i$ . The system of equations is supplemented by the boundary conditions specified in Appendix A of Nayakshin & Melia (1998). The system of equations (4) is in tridiagonal form and can be easily solved to find the electron distribution at time  $t^{n+1}$ . In order to evaluate the energy exchange and dispersion coefficients  $a_i^{n+1}$  and  $D_i^{n+1}$  the code performs an energy balance calculation to find the average electron energy in the ensemble after the current time step, which is then used to calculate the energy exchange and dispersion coefficients due to Møller scattering. All other coefficients are assumed to evolve sufficiently slowly so that the coefficients evaluated under the conditions at the beginning of the current time step can be used.

The implicit scheme of Eq. 4 is known to approach the equilibrium solution for the electron distribution exactly, although the temporal evolution calculated this way becomes inaccurate on short time scales. Since in the problems of interest here, the electron distributions typically evolve on timescales much shorter than the photon distributions, the electrons always attain a distribution close to local equilibrium during each photon time step. Hence, the degree of accuracy provided by the implicit scheme is sufficient for our purposes. As an option, the code can perform the same simulations using an explicit scheme to solve the Fokker-Planck equation. In all test cases, both schemes produced virtually identical results, but the implicit scheme executes a factor of  $\sim 10 - 100$  faster because of the larger individual Fokker-Planck time steps allowed in this scheme.

However, we did not find an appropriate method to calculate the coefficients for the pair production and annihilation rates at time step  $n + 1$ . For this reason, we have to correct the electron and positron distribution functions for pair production and annihilation in an explicit manner. This becomes obviously inaccurate in the case of strongly pair producing model situations. Thus, our scheme is a significant improvement over existing schemes only for pair

deficient situations with pair fractions  $f_{\text{pair}} \equiv n_{e+}/n_p \lesssim$  a few %. For strongly pair dominated situations, we would have to adjust the individual time steps of our simulations so far that such simulations would take a prohibitive amount of computing time.

In the present paper, we focus on results for equilibrium situations, for which we let the code evolve until a stable electron distribution and photon output spectrum is reached. Detailed tests and applications of the time-dependent features of the code will be presented in future publications.

### 3. Tests of the numerical scheme and comparison with Previous Results

For verification of our code, we have first compared the individual energy exchange and diffusion rates,  $d\gamma/dt$  and  $D(\gamma)$ , with those obtained in earlier work. Our numerical energy exchange and diffusion rates due to Coulomb scattering are in agreement with those of Dermer & Liang (1998)<sup>3</sup>. The numerical values of the Møller scattering energy exchange and diffusion coefficients were found in good agreement with those of Nayakshin & Melia (1998)<sup>4</sup>.

We have verified that in cases in which radiative cooling and hydromagnetic acceleration are inefficient, our Fokker-Planck scheme correctly produces a thermal electron distribution in temperature equilibrium with the protons.

In the analysis of coronal energy and radiation transfer, it is customary to parametrize energy input and dissipation rates  $\dot{u}$  [ergs cm<sup>-3</sup> s<sup>-1</sup>] by the dimensionless compactness,  $l$ , which in spherical geometry, is defined by  $l_{\text{sph}} \equiv 4\pi\sigma_T R^2 \dot{u}/(3m_e c^3)$ , where  $R$  is the radius of the spherical volume. In slab geometry, this becomes  $l_{\text{slab}} \equiv \sigma_T H^2 \dot{u}/(m_e c^3)$ , where  $H$  is the thickness of the slab. In our simulations, we specify the heating mechanisms to be Coulomb heating through the thermal protons and resonant wave-particle interactions. Thus, leaving the shape of the electron spectrum general, we calculate the respective energy dissipation rates as

$$\dot{u}_{\text{Coul/A}} = m_e c^2 \int_1^\infty d\gamma n_e(\gamma) \left( \frac{d\gamma}{dt} \right)_{\text{Coul/A}}, \quad (5)$$

where the subscript 'Coul/wp' stands for Coulomb scattering and wave-particle interaction, respectively. Obviously, the resulting compactness will depend not only on the energy density in protons and magnetic turbulence, but also on the current electron distribution (i.e. temperature, if the distribution is predominantly thermal), and can thus not be specified a priori as a free parameter. For comparison with previous work, we need to find appropriate values of the

---

<sup>3</sup>note that in their Eq. (A2), the last  $\gamma^*$  has to be replaced by  $(\gamma^*)^2$

<sup>4</sup>note that there is a '-' sign missing in front of the term  $\propto (\gamma - \gamma_1)^2$  in their Eq. (35)

ion temperature and the wave turbulence amplitude in order to reproduce the dissipation compactness quoted in those papers. We define the temperature corresponding to the electron spectrum resulting from our simulations by requiring that the average electron Lorentz factor,  $\langle \gamma \rangle = (1/n_e) \int d\gamma \gamma n_e(\gamma)$ , be equal to the average Lorentz factor of a thermal electron population of the respective temperature,

$$\langle \gamma \rangle_{\text{th}} = \frac{K_3 \left( \frac{1}{\Theta_e} \right)}{K_2 \left( \frac{1}{\Theta_e} \right)} - \Theta_e. \quad (6)$$

To test our energy balance calculations, we have performed a series of simulations to reproduce the results of the slab corona model of Dove et al. (1997), in particular the inset of their Fig. 2, with which we find good agreement. For those simulations, we specified ion temperatures of  $80 \text{ MeV} \lesssim kT_i \lesssim 250 \text{ MeV}$ , a magnetic field in equipartition with the ion population, and a negligibly low level of Alfvén wave turbulence to reproduce various values of the local heating compactness  $l_c$ . As mentioned earlier, our code is rather inefficient in simulating strongly pair-producing, high- $l_c$  situations because of the explicit scheme to solve for pair balance. For this reason, we restrict the applications of the code in its present version to model situations with pair fractions  $\lesssim$  a few %.

Li et al. (1996a, b) have developed a code solving simultaneously the Fokker-Planck equations for both the electron and the photon distributions in a homogeneous medium, including Coulomb interactions, thermal bremsstrahlung, Compton scattering, resonant wave-particle interactions, and pair production and annihilation. There are two major differences between their approach and ours: (1) We use a Monte-Carlo method to solve the photon transport, and (2) we solve the Fokker-Planck equation for the entire electron spectrum, while Li et al. (1996a, b) split the electron distribution up into a thermal “bath” plus a non-thermal tail, assuming a priori that electrons of energies  $\gamma < \gamma_{\text{thr}} = 1 + 4\Theta_e$  attain a thermal distribution, and that acceleration due to wave/particle interactions affects only particles beyond  $\gamma_{\text{thr}}$ . The latter simplification is justified by the argument that at low electron energies the thermalization time scale is much shorter than any other relevant time scale, and that long-wavelength plasma waves, with which low-energy electrons resonate preferentially, are strongly damped and in energy equilibrium with the thermal pool of electrons. In our simulations, both effects are taken into account self-consistently without making the a-priori assumption of the existence or development of a non-thermal population.

Li et al. (1996b) present two model calculations to explain hard tails observed in the hard X-ray / soft  $\gamma$ -ray spectra of Cyg X-1 and GRO J0422+32. A spherical region of radius  $R = 1.2 \times 10^8 \text{ cm}$  is assumed. For the case of Cyg X-1, they specify a total heating compactness of  $l = 4.5$ , and a non-thermal heat input into suprathermal particles ( $\gamma > \gamma_{\text{thr}}$ ) of  $l_{\text{st}}/l = 0.15$ , with a turbulence amplitude of  $\delta^2 = 0.059$ . A soft blackbody radiation component at  $kT_s = 0.1 \text{ keV}$  from the outer boundary of the sphere is assumed to provide a soft radiation compactness of  $l_s/l = 0.07$ . The seed Thomson depth of the region is  $\tau_p = 0.7$ . In their simulations, Li et al. (1996b) find a

significant suprathermal tail in the resulting electron distribution, which leads to an excess hard X-ray / soft  $\gamma$ -ray emission, consistent with the observed one. The temperature of the thermal part of their electron ensemble is found at  $kT_e = 139$  keV, and the equilibrium pair fraction is  $f_{\text{pair}} \approx 1.8\%$ . For the case of GRO J0422+32 they specify  $l = 0$ ,  $l_{\text{st}}/l = 0.06$ , and  $l_s/l = 0.08$ . This resulted in a weaker nonthermal electron tail, an equilibrium temperature of  $kT_e = 133$  keV, a wave amplitude of  $\delta^2 = 0.065$ , and a pair fraction of  $f_{\text{pair}} \approx 3\%$ .

For comparison with our code, we have run simulations with the same total compactness  $l$ , soft compactness  $l_s$ , soft blackbody temperature  $kT_{\text{BB}}$ , radius  $R$ , seed Thomson depth  $\tau_p$ , and the same values of the plasma wave amplitude normalization  $\delta^2$ . A difficulty in comparing the two codes is that in Li et al. (1996a, b) the ion temperature and magnetic field are not specified explicitly. In our comparative simulations we assume a magnetic field in equipartition with the ion energy density. The results of our simulations are illustrated in Figs. 1 and 2. Our results are qualitatively similar to those of Li et al. (1996a, b). However, we find somewhat lower equilibrium temperatures and stronger nonthermal electron tails as well as stronger suprathermal acceleration compactnesses  $l_{\text{st}}$ . The lower temperatures may be attributed to a rather prominent cyclotron/synchrotron cooling (comparable to Compton cooling) in our simulations (see Figs. 1b and 2b). This, in combination with the larger  $l_{\text{st}}$  values, seems to indicate that in our simulations we have used higher magnetic field values than Li et al. (1996a, b). However, even abandoning the equipartition assumption, we could not find self-consistent parameter values resulting in the same combination of input parameters used by Li et al. (1996a, b). Given this discrepancy in the way of input parameter specification, the qualitative agreement between the results of the two codes, using very different numerical methods, is encouraging.

#### 4. Current Models

We idealize the accretion plasma at the Alfvén radius of disk accretion onto a magnetized neutron star as part of a spherical shell whose distance, magnetic field, and column thickness are fixed by the accretion rate (Ghosh & Lamb 1979a,b, 1990). The distance  $r_0$  is given by

$$r_0 = 2 \times 10^8 f \mu_{30}^{4/7} l_*^{-2/7} M_*^{-1/7} R_6^{-2/7} \text{ cm} \quad (7)$$

where  $\mu_{30} = (\text{neutron star magnetic moment})/(10^{30} \text{ G cm}^3)$ ,  $l_* = L/L_{\text{Edd}}$ ,  $M_* = M_{\text{NS}}/M_{\odot}$ , and  $R_6 = R_{\text{NS}}/(10^6 \text{ cm})$ . For the current simulations, for definiteness, we fix the Ghosh-Lamb fudge parameter  $f = 0.3$ , and set  $M_* = R_6 = 1$ . Hence, the dipole magnetic field at the Alfvén radius is

$$B_0 = 4.2 \times 10^6 l_*^{6/7} \mu_{30}^{-5/7} M_*^{3/7} R_6^{6/7} f^{-3} \text{ G.} \quad (8)$$

The virial ion temperature at  $r_0$  is

$$kT_i = \frac{2}{3} \frac{G M m_H}{r_0} \approx 9.3 \left( \frac{r_0}{10^7 \text{ cm}} \right)^{-1} M_* \text{ MeV.} \quad (9)$$

The column density of the shell can be estimated using the poloidal accretion rate  $\dot{M} \sim 4\pi r_0 \Delta r_0 n_i v_p m_H$ , where we assume that the poloidal velocity  $v_p \sim v_{\text{ff}}/2$  with  $v_{\text{ff}}$  being the free-fall velocity. Hence, the radial Thomson depth of the shell is approximately:

$$\tau_T = \Delta r_0 n_i \sigma_T \sim \frac{\dot{M} \sigma_T}{2\pi r_0 v_{\text{ff}} m_H} \approx 0.97 l_*^{8/7} \mu_{30}^{-2/7} M_*^{4/7} R_6^{1/7} f^{-1/2}. \quad (10)$$

The neutron star (taken to be a 10 km spherical surface) is assumed to emit a blackbody luminosity at the temperature  $kT_{\text{BB}} = 1.78 l_*^{1/4}$  keV. In addition the level of wave turbulence is specified by the dimensionless amplitude  $\delta^2 = (\Delta B/B)^2$  and the spectral index  $q$ . The minimum wavevector  $k_{\min}$  is set to  $2\pi/(\Delta r_0)$ , where  $\Delta r_0 \sim 0.1 r_0$  is the shell thickness (Ghosh & Lamb 1979a,b, 1990). Due to spherical symmetry of our simulations the magnetic field is assumed to be nondirectional in the shell and the synchrotron emissivities and absorption coefficients are angle-averaged.

We have explored the parameter space by varying the accretion rate — corresponding to a variation of the parameter  $l_*$  —, the magnetic field — corresponding to a variation of  $\mu_{30}$  —, and the amplitude of wave turbulence,  $\delta^2$ .  $q$  is set = 5/3 in all runs presented in this paper.

In Fig. 3, we demonstrate the effect of a varying accretion rate in the case of no turbulence,  $\delta^2 = 0$ , and for a fixed magnetic moment of the neutron star,  $\mu_{30} = 1$ , corresponding to a strong surface field of  $B_{\text{surf}} \sim 10^{12}$  G. As the accretion rate decreases, the Alfvén radius moves outward, implying a lower magnetic field at the Alfvén radius, and a lower ion temperature and Thomson depth of the active shell. At the same time, however, Compton cooling becomes less efficient due to the reduced soft photon luminosity of the neutron star surface and due to the larger distance of the active region from the surface. This reduction of the soft photon compactness leads to an increasing equilibrium electron temperature in the accretion shell. Consequently, as the accretion rate decreases, the photon spectra change in the following way: For  $l_* = 1$ , the hard X-ray spectrum smoothly connects to the peak of the thermal blackbody bump from the neutron star surface, and shows a quasi-exponential cutoff at high energies. For lower  $l_*$ , the spectrum turns into a typical low-hard state spectrum of X-ray binaries with the thermal bump clearly distinguished from a hard power-law + exponential cutoff at high energies. The hard X-ray power-law becomes harder with decreasing  $l_*$ . Fig. 4 shows the same sequence of decreasing  $l_*$  for  $\mu_{30} = 10^{-3}$ , corresponding to  $B_{\text{surf}} \sim 10^9$  G. At high accretion rates, a strong reduction of the equilibrium electron temperature with respect to the strong-field case results, leading to a softening of the photon spectrum with decreasing  $\mu_{30}$ . This is due to the *increasing* magnetic field at the Alfvén radius as the neutron star magnetic moment *decreases* (because the Alfvén radius decreases, overcompensating for the decreasing magnetic moment, see Eq. 8), resulting in a lower electron temperature caused due to increasing cyclotron/synchrotron cooling. For low accretion rates ( $l_* \lesssim$  a few %) the electron and photon spectra for the strong-field case and the low-field case are virtually indistinguishable from each other.

Figs. 5 and 6 illustrate the effects of a varying accretion rate and turbulence level on the electron and photon spectra. An increasing turbulence level, obviously, leads to a more pronounced nonthermal tail or bump in the electron spectrum. At the same time, as a result of increased Compton cooling on synchrotron photons produced by the nonthermal electrons, the temperature of the quasi-thermal portion of the electron spectrum decreases as the turbulence level is increasing. Consequently, the photon spectrum at soft to medium-energy X-rays becomes softer with increasing  $\delta^2$ , while at hard X-ray and  $\gamma$ -ray energies an increasingly hard tail develops. As in the case without turbulence, a decreasing accretion rate leads to a higher electron temperature and the transition from a smoothly connected thermal blackbody + thermal Comptonization power-law spectrum to a typical low/hard state X-ray binary spectrum.

Fig. 7 demonstrates the moderate dependence, in particular of the resulting photon spectra, on the magnetic moment of the neutron star for an intermediate value of the accretion rate,  $l_* = 0.25$ . Nonthermal tails in the electron spectra become more pronounced with increasing neutron star magnetic moment. For the weak-field case with  $\mu_{30} = 10^{-3}$ , we find that the high-energy end of the electron spectra are always truncated with respect to a thermal distribution due to strong Compton losses, rather than developing a non-thermal tail.

At very low accretion rates, resulting in very low proton and electron densities in the accretion shell, we find that even at low turbulence level the heating due to stochastic acceleration strongly dominates over Coulomb heating. Consequently, the resulting electron spectrum becomes strongly non-thermal. We need to point out that in those cases, our treatment is no longer self-consistent since in our code the attenuation of Alfvén waves is calculated under the assumption that it is dominated by Landau damping in a thermal background plasma.

## 5. Summary and Conclusions

We have reported on the development of a new, time-dependent code for radiation transport and particle dynamics. The radiation transport, accounting for Compton scattering, bremsstrahlung emission and absorption, cyclotron and synchrotron emission and absorption, and pair processes, is done using a Monte-Carlo method, while the electron dynamics, including radiative cooling, Compton heating/cooling, and stochastic acceleration by resonant interaction with Alfvén/whistler wave turbulence, are calculated using an implicit Fokker-Planck scheme, coupled to the Monte-Carlo radiation transfer code.

In this paper, we have applied our code to the static situation of a shell at the Alfvén radius of a magnetized neutron star. The main results we have obtained are:

(1) The lepton thermal temperature increases, and the hard X-ray photon spectrum becomes harder as the accretion rate is decreasing. At the same time, the normalization of the hard X-ray power-law, relative to the thermal blackbody from the neutron star surface, becomes smaller.

(2) The nonthermal tails in the electron and photon spectra become more dominant and harder as the turbulence level is increasing. At the same time, the quasi-thermal electron temperature decreases, leading to a softer hard-X-ray spectrum.

(3) For low accretion rates ( $\lesssim$  a few %), the photon spectra are only very weakly dependent on the magnetic moment of the neutron star. For higher accretion rates, an increasing neutron star magnetic moment leads to a moderate hardening of the hard X-ray spectrum.

The work of MB is supported by NASA through Chandra Postdoctoral Fellowship Award No. 9-10007, issued by the Chandra X-ray Center, which is operated by the Smithsonian Astrophysical Observatory for and on behalf of NASA under contract NAS 8-39073. This work was partially supported by NASA grant NAG5-4055.

### A. Estimate of equilibrium temperature

The code outlined above can be used for equilibrium situations by simply letting it evolve until both the photon and electron distributions have relaxed to a steady state. In order to provide a consistency test of our numerical methods, we compute a quasi-analytical estimate for the expected equilibrium electron temperature. In our equilibrium simulations, we use this estimated equilibrium temperature as initial condition in order to accelerate the convergence.

Assuming that the electron distribution is roughly thermal, we may estimate the heating and cooling rates due to the various processes as follows. Let

$$W = \frac{1}{n_e} \frac{dE}{dV} = \frac{3}{2} k T_e \quad (\text{A1})$$

be the average energy per electrons. We approximate the cyclotron emissivity by the high-frequency continuum limit given in Mahadevan et al. (1996):

$$j_\nu(\Theta_e) = \frac{2^{1/6}}{3^{5/6}} \frac{\pi^{3/2} e^2 n_e \nu}{c K_2 \left( \frac{1}{\Theta_e} \right) v^{1/6}} \exp \left[ - \left( \frac{9v}{2} \right)^{1/3} \right], \quad (\text{A2})$$

where  $\Theta_e = kT_e/(m_e c^2)$ ,  $v \equiv \nu/(\nu_c \Theta_e^2)$ , and  $\nu_c = eB/(2\pi m_e c)$ .

Denoting by  $\Delta R$  the thickness of the emitting shell or slab, the synchrotron-self-absorption frequency is then determined by solving for

$$1 = \Delta R \kappa_{\text{SSA}} = \Delta R \frac{j_\nu(\Theta_e)}{B_\nu(\Theta_e)}. \quad (\text{A3})$$

The cyclotron/synchrotron cooling rate may then be estimated as

$$\left(\frac{dW}{dt}\right)_{\text{sy}} = \frac{1}{n_e V} \left( A_{\text{surface}} \int_0^{\nu_{\text{SSA}}} d\nu B_\nu(\Theta_e) + V \int_{\nu_{\text{SSA}}}^{\infty} d\nu j_\nu(\Theta_e) \right), \quad (\text{A4})$$

where  $V$  and  $A_{\text{surface}}$  are the volume and the surface area of the emitting shell or slab.

Assuming that the photon field inside the emitting volume is dominated by low-energy photons with  $\epsilon \ll \Theta_e$ , where  $\epsilon = h\nu/(m_e c^2)$ , the Compton cooling rate may be approximated as

$$\left(\frac{dW}{dt}\right)_{\text{IC}} = -4c \sigma_T u_{\text{ph}} \Theta_e \frac{K_3\left(\frac{1}{\Theta_e}\right)}{K_2\left(\frac{1}{\Theta_e}\right)}. \quad (\text{A5})$$

The photon energy density  $u_{\text{ph}}$  is calculated iteratively from the contributions of the various soft photon fields, and repeated Compton scatterings: Assume that the soft photon energy density  $u_s = u_{\text{sy}} + u_{\text{br}} + u_{\text{ext}}$  (synchrotron + bremsstrahlung + external radiation field) is centered around a soft photon energy  $\bar{\epsilon}_s$ , and that  $\tau_T \lesssim 1$ . The average energy change of a photon with mean photon energy  $\bar{\epsilon}_k$  (Compton scattered  $k$  times) changes on average by a factor  $\Delta\bar{\epsilon}_k = \bar{\epsilon}_k (4\Theta_e - \bar{\epsilon}_k)$  in the course of the  $k+1$ . scattering. Then, the total internal photon energy density is

$$u_{\text{ph}} = u_s \left( 1 + \sum_{n=1}^{\infty} \tau_T^n \prod_{k=0}^{n-1} [4\Theta_e - \bar{\epsilon}_k] \right), \quad (\text{A6})$$

where  $\bar{\epsilon}_0 = \epsilon_s$  and  $\bar{\epsilon}_{k+1} = \bar{\epsilon}_k (1 + 4\Theta_e - \bar{\epsilon}_k)$ .

In the cases we are interested in, the bremsstrahlung photon input will be negligible compared to cyclotron/synchrotron and the external soft photon fields. Thus, we assume  $u_s = u_{\text{ext}} + u_{\text{sy}}$  with

$$u_{\text{ext}} = \frac{F_{\text{ext}}}{c} \quad (\text{A7})$$

and

$$u_{\text{sy}} = \frac{1}{c} \int_0^{\nu_{\text{SSA}}} d\nu B_\nu(\Theta_e) + \frac{\Delta R}{c} \int_{\nu_{\text{SSA}}}^{\infty} d\nu j_\nu(\Theta_e). \quad (\text{A8})$$

The photon energy  $\bar{\epsilon}_s$  is  $\bar{\epsilon}_{\text{ext}}$  if  $u_{\text{ext}} > u_{\text{sy}}$ , or  $\max\{\epsilon_{\text{SSA}}, \epsilon_0\}$  else, where  $\epsilon_0 = (h\nu_c/m_e c^2)$ .

The bremsstrahlung cooling rate is

$$\left(\frac{dW}{dt}\right)_{\text{br}} = - \begin{cases} \frac{128}{3\sqrt{\pi}} \alpha r_e^2 m_e c^3 n_e \sqrt{\Theta_e} & \text{for } \Theta_e \ll 1 \\ 96 \alpha r_e^2 m_e c^3 n_e \Theta_e (\ln[2\Theta_e] + 0.673) & \text{for } \Theta_e \gtrsim 1 \end{cases} \quad (\text{A9})$$

(Haug 1985) where  $\alpha = 1/137$  is the fine structure constant and  $r_e$  is the classical electron radius.

The heating rate due to Alfvén wave turbulence is either specified as a fixed parameter, or can be evaluated using the acceleration rates according to Eq. (2) as

$$\left( \frac{dW}{dt} \right)_A = m_e c^2 \int_1^\infty d\gamma \dot{\gamma}_A f_e(\gamma). \quad (\text{A10})$$

Finally, the Coulomb heating / cooling rate is

$$\left( \frac{dW}{dt} \right)_{\text{Coul}} = \frac{3}{2} \frac{m_e}{m_p} \ln \Lambda n_p c \sigma_T (kT_p - kT_e) h(\Theta_e, \Theta_p), \quad (\text{A11})$$

where

$$h(\Theta_e, \Theta_p) = \frac{\sqrt{\Theta_e}}{(\Theta_e + \Theta_p)^{3/2}} \frac{2(\Theta_e + \Theta_p)^2 + 2(\Theta_e + \Theta_p) + 1}{K_2\left(\frac{1}{\Theta_e}\right)} \exp\left(-\frac{1}{\Theta_e}\right) \quad (\text{A12})$$

(Dermer 1986),  $\ln \Lambda$  is the Coulomb logarithm,  $n_p$  is the number density of ions, and  $\Theta_p = kT_p/(m_p c^2)$ .

The total heating/cooling rate consists the sum of all elementary processes,

$$\left( \frac{dW}{dt} \right)_{\text{total}} = \left( \frac{dW}{dt} \right)_{\text{Coul}} + \left( \frac{dW}{dt} \right)_A + \left( \frac{dW}{dt} \right)_{\text{sy}} + \left( \frac{dW}{dt} \right)_{\text{IC}} + \left( \frac{dW}{dt} \right)_{\text{br}}, \quad (\text{A13})$$

and we are iteratively solving for the equilibrium solution(s) with  $\left( \frac{dW}{dt} \right)_{\text{total}} = 0$ .

## REFERENCES

Böttcher, M., & Liang, E. P., 1998, ApJ, 506, 281  
 Böttcher, M., Pohl, M., & Schlickeiser, R., 1999, Astrop. Phys., 10, 47  
 Böttcher, M., & Schlickeiser, R., 1997, A&A, 325, 866  
 Dermer, C. D., 1986, ApJ, 307, 47  
 Dermer, C. D., & Liang, E. P., 1989, ApJ, 339, 512  
 Dove, J. B., Wilms, J., & Begelman, M. C., 1997, ApJ, 487, 747  
 Ghosh, P., & Lamb, F., 1979a, ApJ, 232, 259  
 Ghosh, P., & Lamb, F., 1979b, ApJ, 234, 296  
 Ghosh, P., & Lamb, F., 1990, in “Neutron Stars”, ed. J. Ventura (Kluwer Acad., Amsterdam)  
 Haug, E., 1985, A&A, 148, 386  
 Li, H., Kusunose, M., & Liang, E. P., 1996a, ApJ, 460, L29

Li, H., Kusunose, M., & Liang, E. P., 1996b, A&AS, 120, 167

Liang, E. P., Böttcher, M., Lin, D., & Smith, I. A., AIP Conf. Proc. 510, 245, ed. McConnell, M. L., & Ryan, J. M. (AIP, New York)

Lightman, A. P., & White, T. R., 1988, ApJ, 335, 57

Mahadevan, R., Narayan, R., & Yi, I., 1996, ApJ, 465, 327

Malzac, J., & Jourdain, E., 2000, A&A, in press

Nayakshin, S., & Melia, F., 1998, ApJS, 114, 269

Rybicki, G. B., & Lightman, A. P., 1979, “Radiative Processes in Astrophysics”, John Wiley & Sons, New York

Schlickeiser, R., 1989, ApJ, 336, 243

Schlickeiser, R., Fichtner, H., & Kneller, M., 1996, JGR, 102, 4725

Stern, B. E., Begelman, M. C., Sikora, M., & Svensson, R., 1995, MNRAS, 272, 291

Svensson, R., 1982, ApJ, 258, 321

Tavani, M., et al., 1996, A&AS, 120, 221

Tavani, M., & Liang, E. P., 1996, A&AS, 120, 133

White, T. R., Lightman, A. P., & Zdziarski, A. A., 1988, ApJ, 331, 939

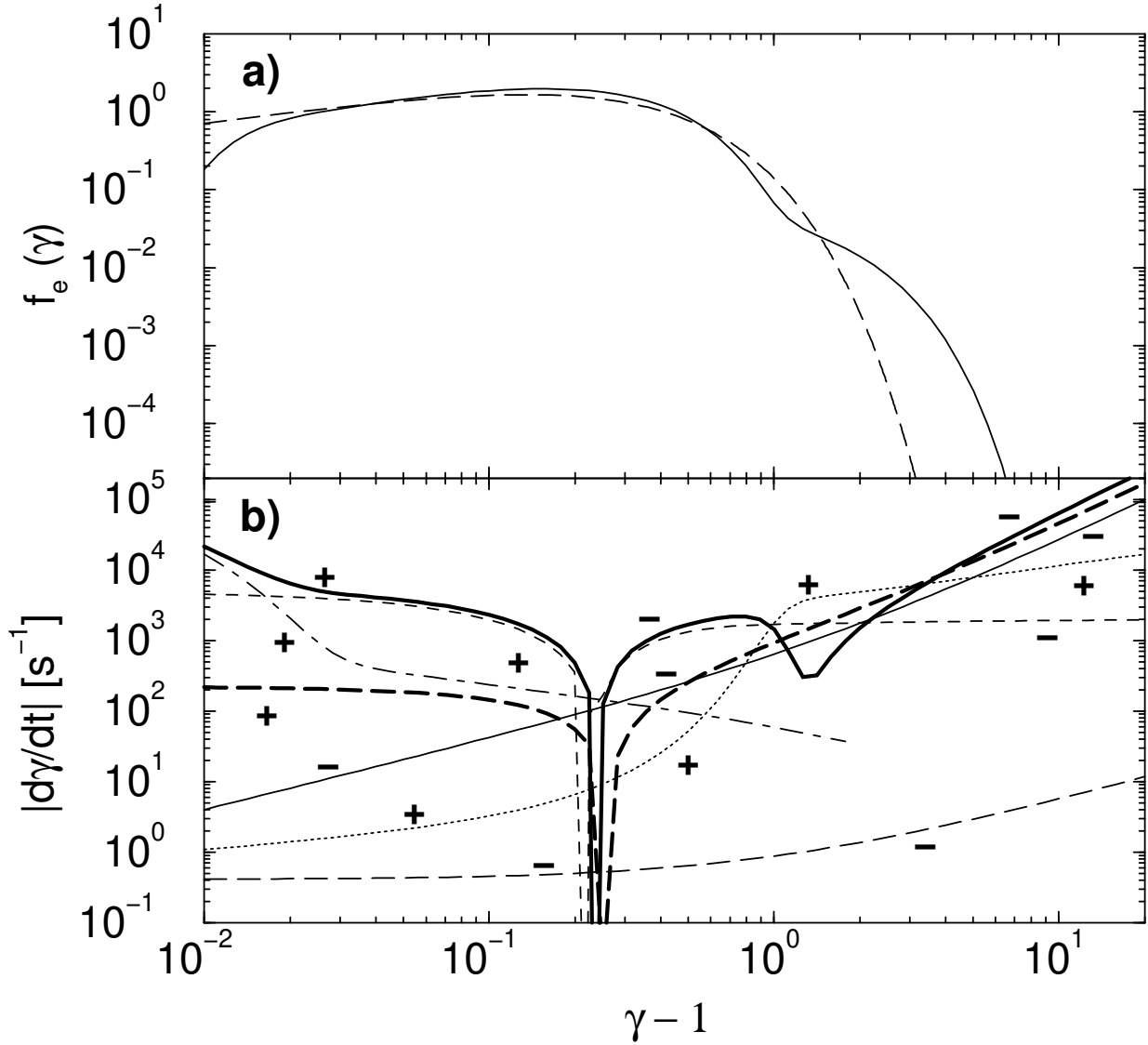


Fig. 1.— Equilibrium electron spectrum (a) and absolute value of the energy exchange coefficients (b) for our model calculation with parameters similar to the Cyg X-1 case of Li et al. (1996b). The labels ‘+’ and ‘-’ in panel (b) indicate the sign of the respective contributions. The individual contributions are: synchrotron (thin solid), bremsstrahlung (thin long-dashed), Compton (thick long-dashed), Coulomb scattering (dot-dashed), Møller + Bhabha scattering (short-dashed), hydromagnetic acceleration (dotted), and total (thick solid). Input parameters were:  $kT_i = 3.5$  MeV,  $\tau_p = 0.7$ ,  $R = 1.2 \cdot 10^8$  cm,  $B = B_{ep} = 1.1 \cdot 10^6$  G,  $\delta^2 = 0.059$ ,  $kT_{BB} = 0.1$  keV,  $l_s = 0.315$ . Resulting equilibrium parameters are  $l = 4.43$ ,  $l_{st}/l = 0.46$ ,  $f_{pair} = 1.7$  %,  $kT_e = 105$  keV. The long-dashed curve in panel (a) is a thermal electron spectrum with  $kT_e = 105$  keV.

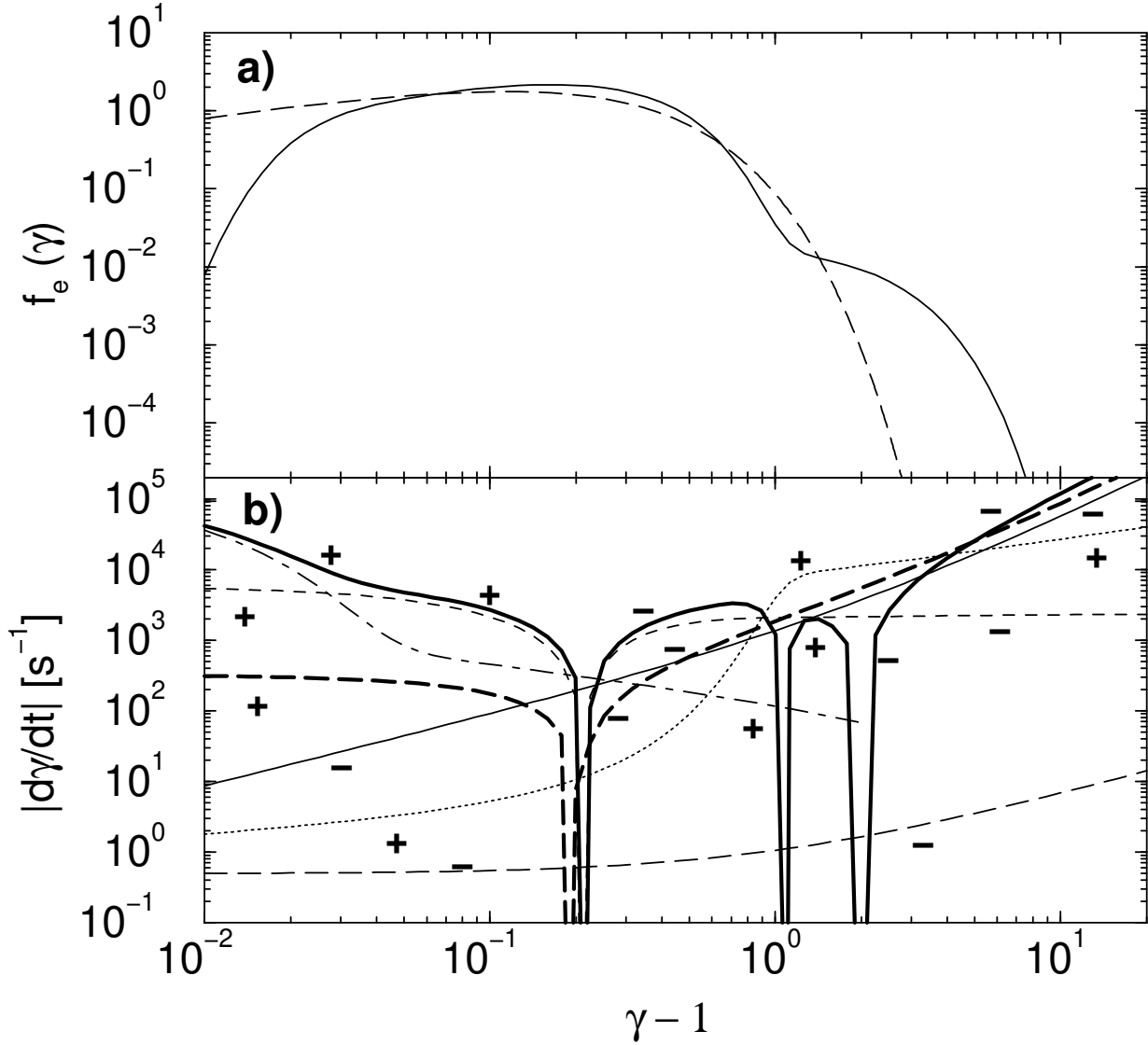


Fig. 2.— Equilibrium electron spectrum (a) and absolute value of the energy exchange coefficients (b) for our model calculation with parameters similar to the GRO J0422+32 case of Li et al. (1996b). The labels ‘+’ and ‘-’ in panel (b) indicate the sign of the respective contributions. The individual contributions are: synchrotron (thin solid), bremsstrahlung (thin long-dashed), Compton (thick long-dashed), Coulomb scattering (dot-dashed), Møller + Bhabha scattering (short-dashed), hydromagnetic acceleration (dotted), and total (thick solid). Input parameters were:  $kT_i = 7.2$  MeV,  $\tau_p = 0.7$ ,  $R = 1.2 \cdot 10^8$  cm,  $B = B_{ep} = 1.65 \cdot 10^6$  G,  $\delta^2 = 0.065$ ,  $kT_{BB} = 0.1$  keV,  $l_s = 0.72$ . Resulting equilibrium parameters are  $l = 8.66$ ,  $l_{st}/l = 0.43$ ,  $f_{pair} = 11\%$ ,  $kT_e = 93$  keV. The long-dashed curve in panel (a) is a thermal electron spectrum with  $kT_e = 93$  keV.

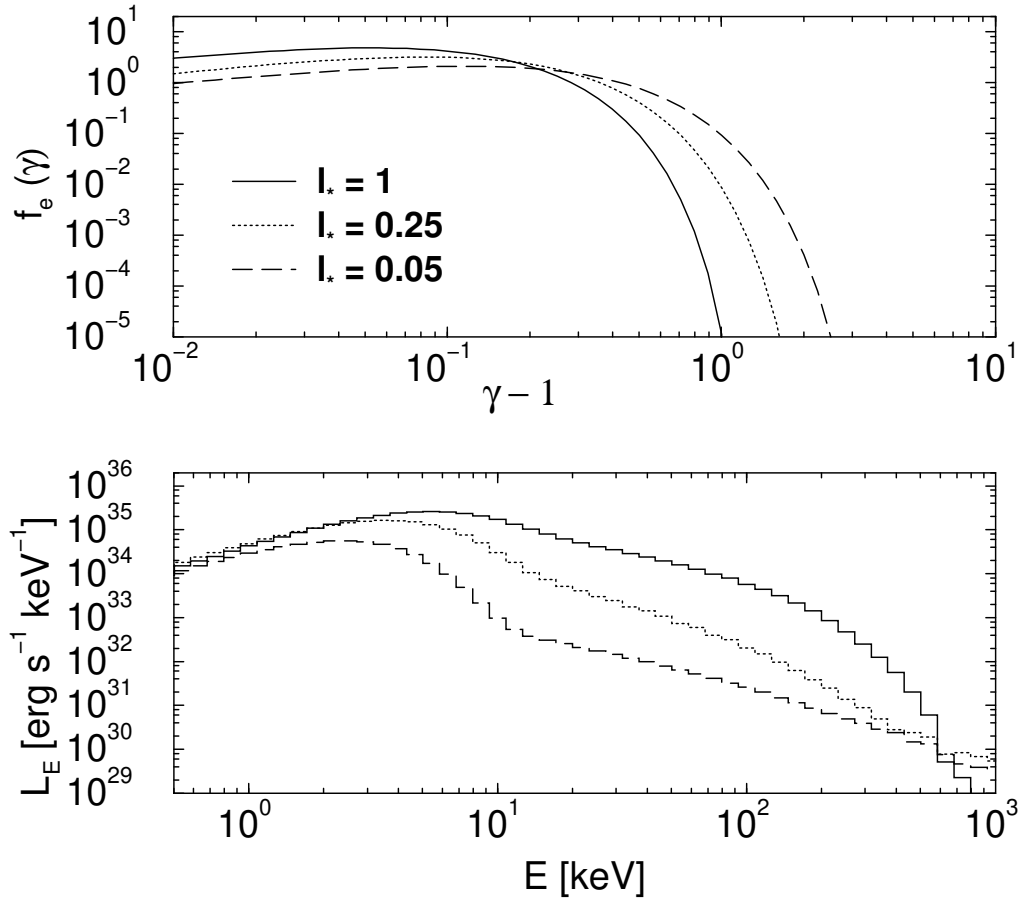


Fig. 3.— Equilibrium electron spectra (top panel) and photon spectra (bottom panel) for fixed pulsar dipole moment  $\mu_{30} = 1$  and no plasma wave turbulence ( $\delta^2 = 0$ ).

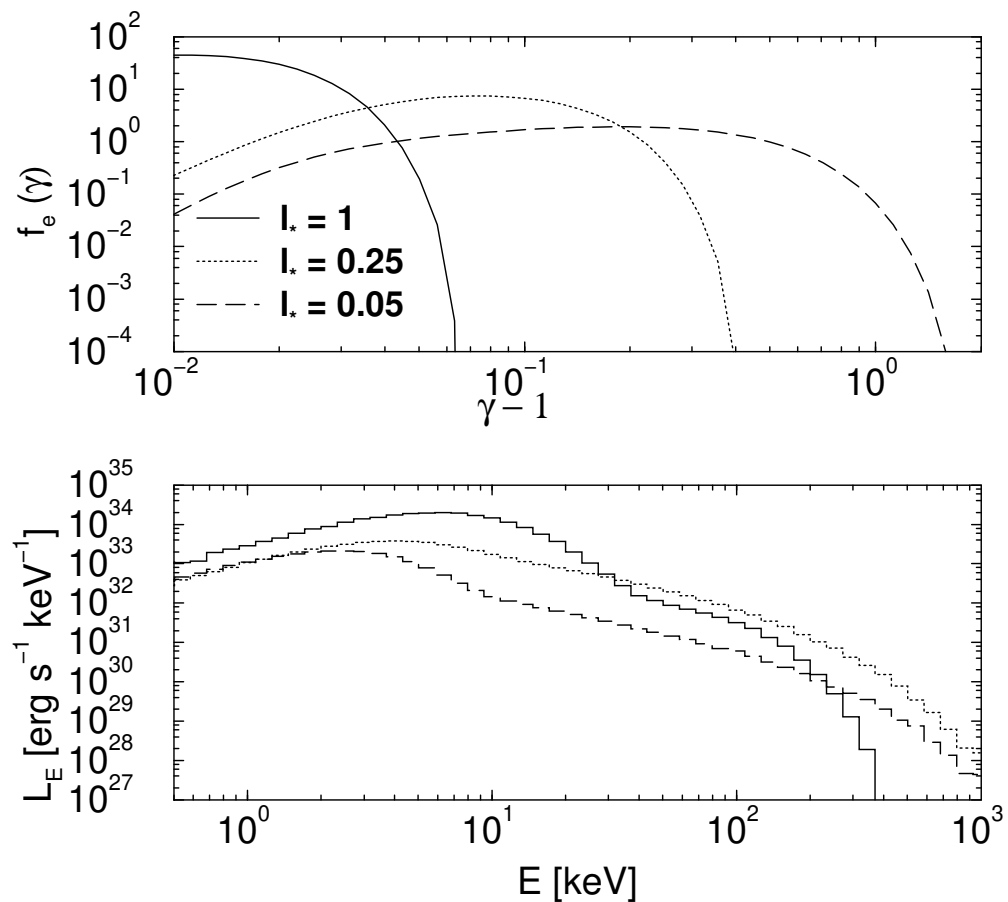


Fig. 4.— Same as Fig. 3, but with  $\mu_{30} = 10^{-3}$ .

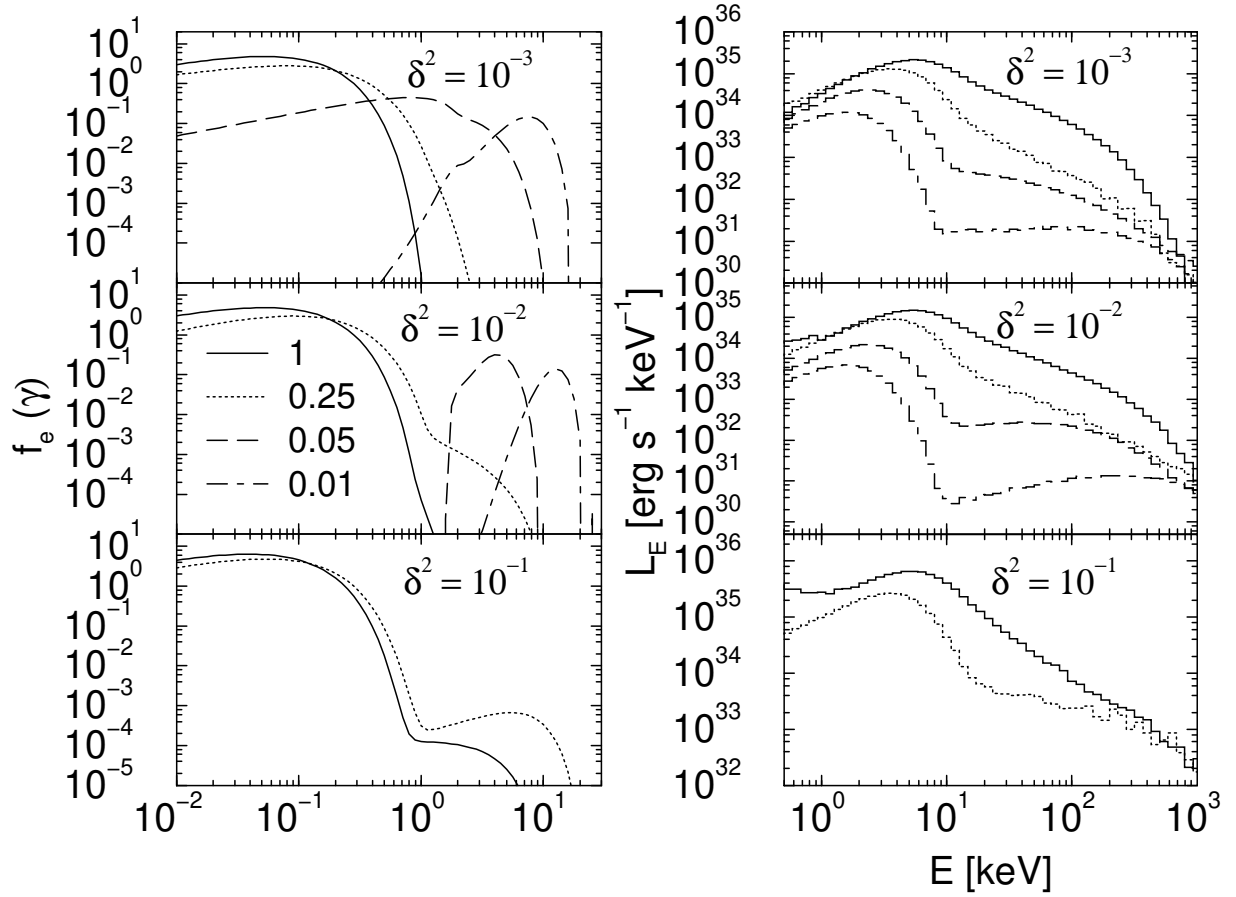


Fig. 5.— Equilibrium electron spectra (left panels) and photon spectra (right panels) for fixed pulsar dipole moment  $\mu_{30} = 1$ . The legend in the upper left panel refers to the values of  $l_*$  used in the individual runs.

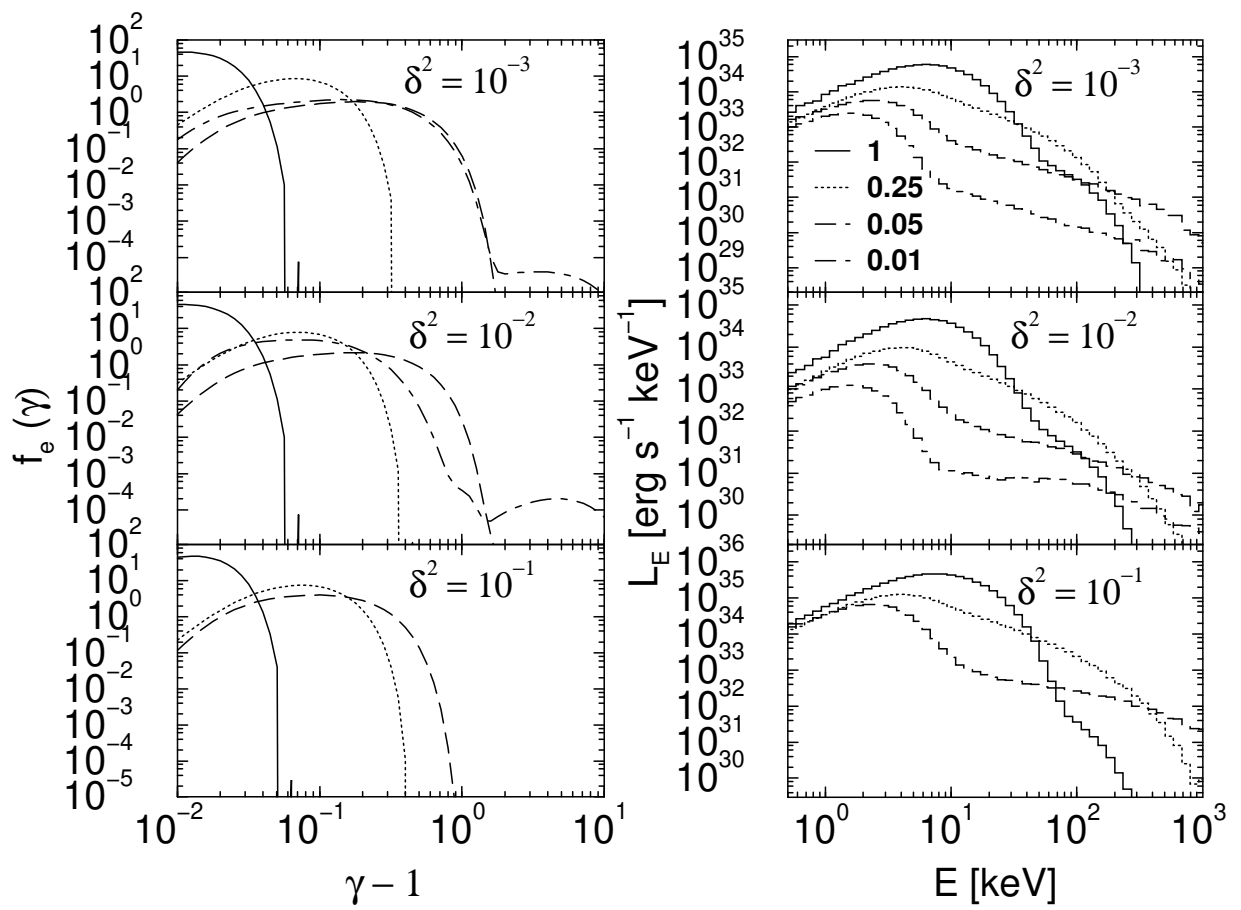


Fig. 6.— Same as Fig. 5, but with  $\mu_{30} = 10^{-3}$ .

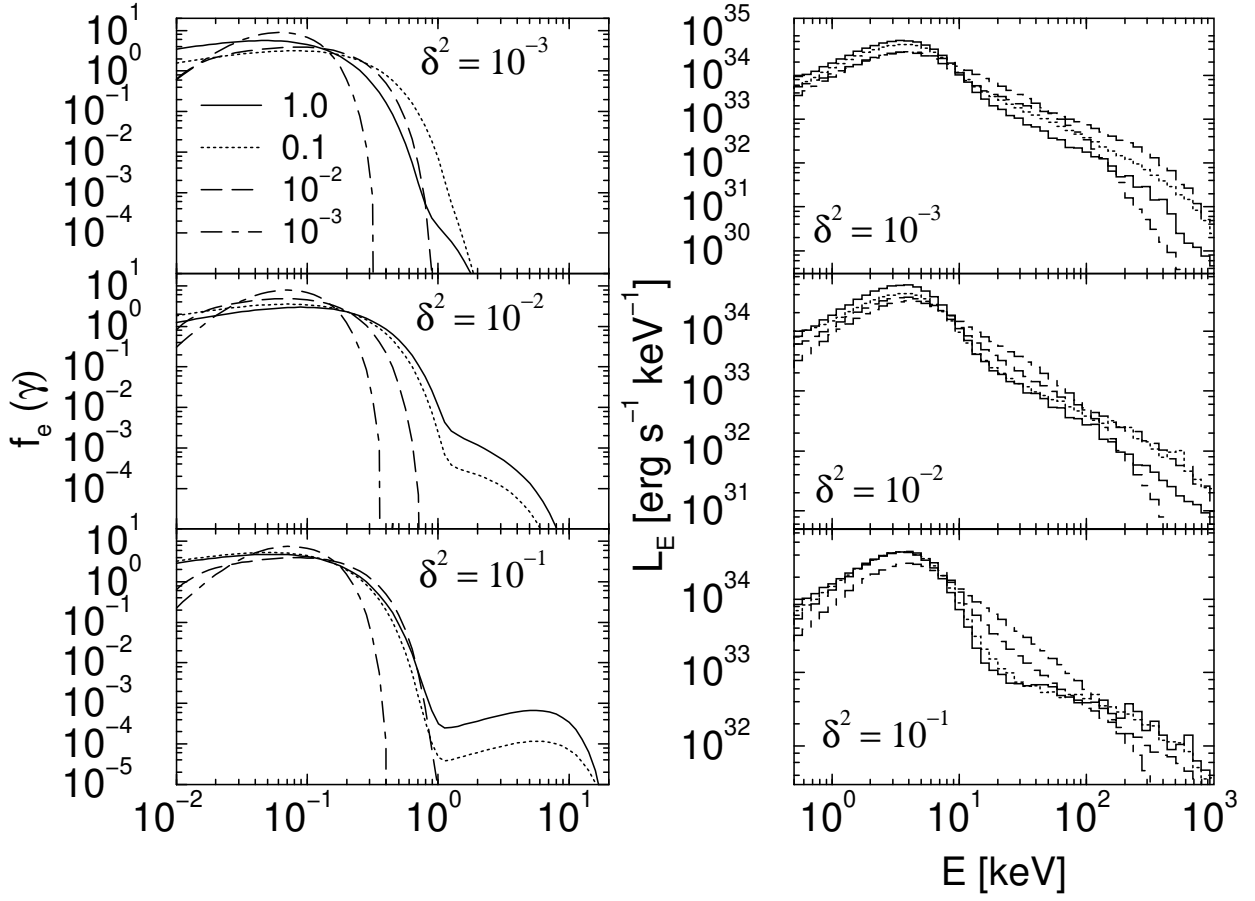


Fig. 7.— Equilibrium electron spectra (left panels) and photon spectra (right panels) for fixed accretion rate and luminosity  $l_* = 0.25$ . The legend in the upper left panel refers to the values of  $\mu_{30}$  used in the individual runs.